Optimal Planning and Guidance for Solar System Exploration using Electric Solar Wind Sails

Javier Urrios[a,*], Guillermo Pacheco-Ramos[a] and Rafael Vazquez[a]

[a]*Department of Aerospace Engineering, Universidad de Sevilla, Seville, Spain*

ARTICLE INFO

Keywords:
Electric Solar Wind Sails
Rendezvous missions
Optimal Planning
Guidance Strategies
Non-Linear Programming
Model Predictive Control

ABSTRACT

Electric Solar Wind Sails (E-Sails) are a new type of spacecraft propellantless propulsion system that gathers its energy from solar wind protons and is potentially useful for interplanetary missions. Although optimal interplanetary trajectories have been the subject of thorough research, the substantial variability of the solar wind necessitates the adoption of active guidance strategies, an area that has received significantly less scholarly attention. This paper proposes guidance algorithms for E-Sails based on Model Predictive Control (MPC), a modern control methodology based on online re-planning of the trajectory. To this end, first, properties of E-sail time-optimal orbits are studied applying Pontryagin's Minimum Principle, and then time-optimal orbits for missions to Mars and Jupiter are computed via direct transcription methods. Next, solar wind perturbations are modeled, posing a challenging saturation problem due to their high variability. Guidance strategies based on Shrinking Horizon and Receding Horizon Model Predictive Control (RHMPC) are developed, analyzed and compared using Monte Carlo simulations, successfully implementing MPC to E-sail guidance. Lastly, the RHMPC strategy is successfully tested with accurate historical solar wind data from the WSA-Enlil model.

1. Introduction

Since the dawn of the Space Age, the exploration of the Solar System has been one of the main drivers of space technology. However, going beyond Earth's closest neighbours is exceedingly challenging due to the enormous energetic costs involved in orbital transfers. This limitation motivated the study of more efficient propulsion methods, such as propellantless systems.

The Electric Solar Wind Sail (E-sail) falls into the broader category of propellantless propulsion systems, a in particular, belongs to those designed to extract from the Sun the energy needed for orbital transfers. The solar sails, also known as photon sails, conceived by K. Tsiolkovsky [1] and F. Tsander [2] among others, use sunlight photons as the source of energy. They work similarly to a sailing boat, hence their name. The idea is to deploy a large reflective surface around the spacecraft to reflect photons from the solar wind. By Maxwell's Theory of Electromagnetism, a resultant force and moment (not necessarily perpendicular to the surface) are exerted on the spacecraft. Therefore, both orbit and attitude can be modified. This type of solar sails is the most common to date; LightSail 2 [3] and IKAROS [4] are examples of successful missions carried out using this technology. Looking ahead, the ACS3 [5] or Solar Cruiser [6] missions are representative of the advancements that can be achieved in the coming years.

Later, in 1988, D. Andrews and R. Zubrin, proposed the concept of magnetic solar sail [7]. It works by creating a magnetic field around the sail that deflects the solar plasma, and therefore extracts its momentum. However, technical challenges in regards to the magnetic field source are still unsolved, and no real mission has used this type of sail yet.

Lastly, the Electric Solar Wind Sail concept, which is the one considered in this article, was initially conceived by P. Janhunen in 2004 [8]. Inspired by the development of photonic solar wind sails, he studied the feasibility of a similar model that produced thrust by modifying the momentum of protons using an electric field generated by a mesh of wires, thus creating repulsive Coulomb forces. From there, many investigations were conducted around its design [9–11], deployment [12], applications [13], thrust modeling [14, 15] and performance [16, 17], among other topics. In terms of the orbital mechanics problem, techniques for computing optimal trajectories [18–21], applications to potentially viable missions [22–25] or basic algorithms for trajectory correction [26, 27] are examples of research carried out. Investigations around attitude dynamics have also been conducted [28, 29], some of the latest related to

*Correspondence to: G. Pacheco-Ramos.
javierurriosg@gmail.com (J. Urrios); gpacheco@us.es (G. Pacheco-Ramos); rvazquez1@us.es (R. Vazquez)
ORCID(s): 0009-0006-9584-2471 (J. Urrios); 0000-0001-9655-7820 (G. Pacheco-Ramos); 0000-0001-6904-2055 (R. Vazquez)

the development of control laws with realistically shaped tethers [30–33], the study of the effects in dynamics and control of important variables such as spin rate using FEMs [34, 35], the deduction of propulsive models taking into account more complex phenomena like coning angle dynamics [36], or the study of tethers' oscillations using dynamic multibody models [37]. In regards to the suitability of this propellantless system, the ESTCube-2 CubeSat is planned to be launched in the second half of 2023, and will serve to demonstrate the E-sail technology.

While the optimal trajectory problem has been extensively studied, the guidance problem due to solar wind uncertainty is a much more challenging problem [38, 39]. Although this problem has been previously tackled by repetitively solving the trajectory indirect problem in [26], this work aims to solve this challenge using conventional control strategies based on Model Predictive Control (MPC). This concept, which originated in the late seventies, is a family of control strategies that use a system model to predict future values of state variables up to a future time horizon in terms of the past and present state and control values, and then minimizes a cost function in order to obtain the optimal future control values. Each sampling time, this process is repeated. MPC is therefore very suited for slow systems that require a robust control due to the presence of significant disturbances. In fact, it has already been considered for spacecraft missions such as rendezvous [40] or attitude control for spacecraft rendezvous [41] or E-sail attitude maneuver [32, 33]. Due to the high solar wind variability, MPC is well-suited for the development of guidance strategies for the E-sail, which is crucial to its applicability, since thrust produced is directly related to solar wind. This fact is of great importance, because until now, solar wind fluctuations interfered with interplanetary spacecrafts as variations in radiation pressure or similar physical phenomena, which were relatively small in terms of magnitude. However, variations in solar wind can potentially double or halve the thrust produced by the E-sail.

This dramatic variability has to be taken into account in the guidance strategy. One of the simplest ways to deal with uncertainty, and the one chosen in this work, is the consideration of worst-case scenarios or safety margins taking into account the distribution of uncertainty. In MPC, similar ideas have been used in the past, by setting the constraints to the worst possible case, see e.g. [42] or using chance constraints from which safety margins are derived [43, 44]. In addition, the scope of robust design methodologies is broad and diverse, offering a multitude of avenues for enhancing guidance robustness in the face of uncertainty. Indeed, the most recent literature contains a variety of such methodologies, such as tube-based MPC [45], direct adaptive control [46], robust learning methods [47], reinforcement learning [48], stochastic optimal control [49], belief Markov decision processes and belief optimal control [50], or robust epistemic uncertainty optimization [50]. These approaches are particularly pertinent when facing indeterminate models of uncertainty, wherein the identification and characterization of uncertainty become essential [42, 45, 51]. Each of these methodologies can contribute in different ways to the robustness of guidance systems, expanding the toolbox available for dealing with for dealing with uncertainty in optimal trajectory design.

The main contributions of this work can be summarized as follows. Firstly, the performance of the guided trajectory problem formulation is evaluated under solar wind uncertainty, employing both shrinking and receding strategies for missions to Mars and Jupiter. Beyond feedback's own ability to reject disturbances, uncertainties are dealt with by using worst-case scenarios and safety margins (taking into account the distribution of solar wind variability), which inevitably leads to sub-optimal solutions. The proposed strategy is applicable to various planetary or interplanetary missions, including destinations within the inner planets. However, Mars and Jupiter are chosen based on the superior performance attributed to the E-sail when operating farther from the Sun compared to other propellantless systems relying on solar wind, owing to its lower decay [16]. Furthermore, a study of the influence of the safety margin for nominal acceleration on trajectory recalculations and its impact on the success rate through Monte Carlo analysis is presented. For the receding horizon strategy, various objective functions are proposed and compared. Finally, the viability of receding horizon MPC is demonstrated by considering time-varying solar wind variations derived from accurate models.

In this work, a two dimensional problem is considered for simplicity and circular orbits are assumed for planet's orbits [16, 39]. Sun-based canonical units are used in the formulation. The cited hypothesis allows to keep the focus on the guidance problem and the solar wind variability by eliminating the influence of the planets' orbits but do not diminish the value of the main contribution of this work. The consideration of a more detailed 3D problem with more realistic orbits has already been assessed for E-sail and its feasibility demonstrated [52].

This paper is organized as follows. Section 2 introduces the models used for orbital motion, E-sail thrust and solar wind uncertainty. Next, Section 3 presents the optimal trajectory planning under nominal solar wind for interplanetary missions to Mars and Jupiter. Subsequently, in Section 4, the formulation of the Shrinking Horizon and Receding Horizon MPC guidance strategies is discussed, taking into account the effects of solar wind uncertainties. Additionally, the results of the Monte Carlo analysis carried out for both approaches are provided. In Section 5, a successful mission

to Mars is computed using actual historical solar wind data and employing the Receding Horizon MPC strategy. Finally, the conclusions drawn from the obtained results are presented in Section 6 and the future works are identified.

2. Models for E-Sail trajectories

In this section a model for the E-sail thrust is introduced and the equations of motion are presented. Next, solar wind uncertainty is introduced and modeled as a probability distribution. Additionally, model limitations and assumptions are also discussed.

For convenience, canonical units are used, with the acronym AU meaning Astronomical Unit, and UV Units of Velocity (that is, AU divided by the canonical Unit of Time UT). In this sense, 1AU $\approx 1.496 \cdot 10^{11}$ m, 1UT ≈ 58.1324 days and 1UV ≈ 29.785 km/s.

2.1. E-sail thrust model

The E-sail thrust model used for this work is the one presented in [14], which is developed from a geometrical standpoint, and proposes simple yet precise expressions of radial and tangential accelerations produced by the E-sail. It should be noted the thrust model is reliable in the solar wind near 1 AU and for typical E-sail parameters. Outside of those conditions, the accuracy of the model may be diminished. The radial and tangential accelerations are given by

$$\begin{aligned} a_r &= \tau \frac{a_c}{2} \left(\frac{r_\oplus}{r}\right) \left(1 + \cos^2 \alpha_n\right), \\ a_\theta &= \tau \frac{a_c}{2} \left(\frac{r_\oplus}{r}\right) \cos \alpha_n \sin \alpha_n. \end{aligned} \tag{1}$$

Note that the acceleration produced by the E-sail is inversely proportional to the distance from the Sun, r . In this model, $\tau \in [0, 1]$, which is a control variable, represents the throttle level of the E-sail, with 0 meaning that no thrust is produced and 1 representing maximum thrust. The value a_c is the spacecraft characteristic acceleration (i.e. the maximum value of acceleration measured at 1AU from the Sun, $r_\oplus$). The sail pitch angle, which is denoted α_n, has an influence not only in the acceleration direction, but also in the modulus. A concept visualization of this thrust model is presented in Fig. 1. In this study, it is assumed that the throttle level and the sail pitch angle can be instantaneously controlled at will, i.e., they are the control variables. In reality, controlling the sail pitch angle presents an attitude problem that is also being addressed (see [30], [34]), although it occurs on a much shorter timescale.

Defining a as the acceleration modulus computed from the components described in Eq. (1), the dimensionless propulsive acceleration modulus, considering $\tau = 1$, is defined as $\gamma = a/\left(a_c \left(r_\oplus/r\right)\right)$ and is represented Fig. 2 as a function of the sail angle α_n. The the thrust cone angle α, is also depicted. There is a maximum value of α_n, which recent studies approximate to be in the range of 60° to 70° [11], since going beyond that limit implies dealing with non-desirable instabilities. However, looking at the evolution of γ, it can be seen that, assuming an optimal transfer, there is no apparent reason for going beyond the sail pitch angle that yields maximum thrust cone angle α^{max} (marked in Fig. 2), since the non-dimensional acceleration γ is strictly decreasing with α_n. The results provided in Section 3.2 corroborate that, for optimal mission planning, the sail angle value remains within the feasible range.

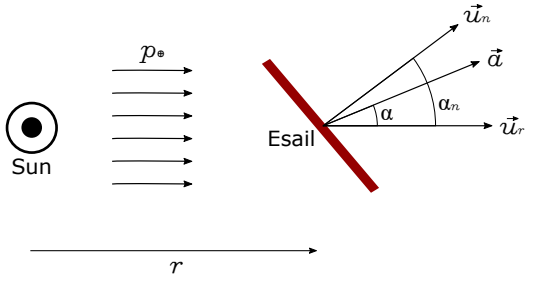

Figure 1: Conceptual E-sail thrust model illustration

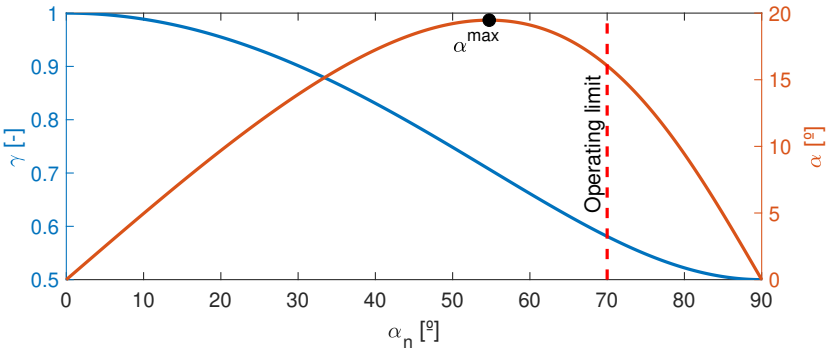

Figure 2: Variation with respect to α_n of γ (in blue) and α (in orange)

2.2. Equations of motion

First, the orbital equation of motion including the E-sail acceleration,

$$\ddot{\boldsymbol{r}} = -\frac{\mu}{r^2}\frac{\boldsymbol{r}}{r} + \boldsymbol{a} + \boldsymbol{a}_p \tag{2}$$

where $\mu = 1.327124 \cdot 10^{11}$ km^3/s^2 is the Standard Gravitational Parameter of the Sun, $\boldsymbol{r}$ denotes the position vector in the Heliocentric Inertial reference frame (HCI), $\boldsymbol{a}$ accounts for the E-sail acceleration and $\boldsymbol{a}_p$ represents the acceleration caused by disturbances, such as third-body perturbations. The equations of motion are obtained by conveniently expressing the equation of motion as a set of first order differential equations expressed in polar coordinates, yielding

$$\begin{aligned}
\dot{r} &= v_r, \\
\dot{\theta} &= \frac{v_\theta}{r}, \\
\dot{v_r} &= \frac{v_\theta^2}{r} - \frac{\mu}{r^2} + \tau\frac{a_c}{2}\left(\frac{r_\oplus}{r}\right)\left(1+\cos^2\alpha_n\right), \\
\dot{v_\theta} &= -\frac{v_r v_\theta}{r} + \tau\frac{a_c}{2}\left(\frac{r_\oplus}{r}\right)\cos\alpha_n \sin\alpha_n.
\end{aligned} \tag{3}$$

Note that perturbations are omitted, which will be taken care of by the closed loop guidance strategy.

2.3. Solar wind uncertainty model

According to [53], the force per unit length exerted by each one of the tethers that make up the E-sail follows the expression

$$f_l = 0.18\max(0, V_0 - V_1)\sqrt{\epsilon_0\, p_\oplus}, \tag{4}$$

where V_0 denotes the tether voltage, V_1 the solar wind electric potential, ϵ_0 is the vacuum permittivity and $p_\oplus$ denotes the dynamic pressure of the Sun at 1 AU distance from it, all expressed in the International System of Units. Since typically $V_0 \gg V_1$, it can be assumed that the force per unit length generated by a tether is proportional to the square root of the dynamic pressure. Moreover, the total force generated by a tether can be computed knowing the force per unit length and applying a correction factor k_1 ($f_t = k_1\, f_l\, l$) which depends on the geometry. Similarly, the total force is obtained by multiplying the force of an individual tether by the number of tethers n_t, and applying another geometric correction k_2 ($F = k_2\, n_t\, f_t$). Therefore, the total force is proportional to the force per unit length, and thus acceleration is proportional to the squared root of the dynamic pressure (i.e. $a \propto p_\oplus^{1/2}$). Thus, the modeling of dynamic pressure uncertainties is crucial, since it directly impacts the performance of the E-sail.

Predicting the dynamic pressure of the Sun is remarkably difficult. The intrinsic chaotic and turbulent processes happening in its interior make the fluctuations of solar wind rather unpredictable [54]. Fig. 3 represents a histogram of the dynamic pressure obtained from data gathered from the NASA OMNIWeb Data Explorer, as proposed in [38]. The

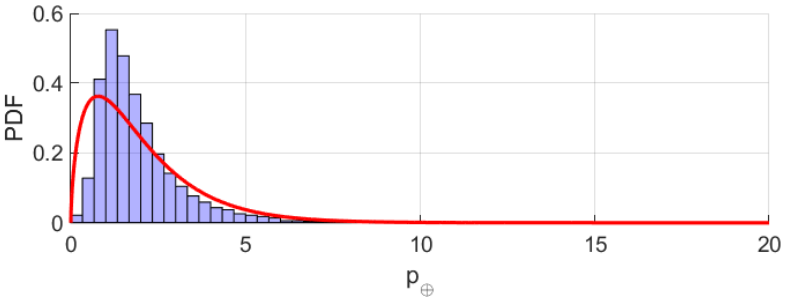

Figure 3: Gamma distribution of $p_\oplus$ (red line) compared with real data gathered from NASA (bars)

mean dynamic pressure at 1 AU can be estimated to be around $\overline{p}_\oplus \approx 2$ nPa, with an standard deviation of approximately $\sigma_{p_\oplus} \approx 1.56$ nPa.

Following [38], the distribution function of the solar wind dynamic pressure at 1AU is approximated by a gamma distribution. A comparative of both the real distribution and gamma approximation can be observed again in Fig. 3. The probability density function of $p_\oplus$ is given by

$$f(p_\oplus) = \frac{\beta^{-\alpha}}{\Gamma(\alpha)} p_\oplus^{\alpha-1} \exp(-p_\oplus/\beta), \tag{5}$$

where the coefficients $\alpha = 1.6437$, $\beta = 1.2168$, are considered to adjust the mean and standard deviation.

As shown in Fig. 3, the gamma probability density function (PDF) tends to overestimate the likelihood of having values of $p_\oplus$ smaller (or slightly greater) than the mean value $\overline{p}_\oplus$. Simultaneously, it underestimates the peak near $\overline{p}_\oplus$ and the values in the tail. This leads to a certain level of conservatism in the considered solar pressure distribution compared to the actual one. It's worth noting that the guidance strategies proposed in this study could potentially be applied to other models of solar pressure PDFs, and better results could be achieved if a more precise uncertainty model is considered [55]. Finally, since the real data for solar wind dynamic pressure available corresponds to 1 AU, it should be acknowledge that the representativeness of the uncertainty model used is anticipated to diminish with increasing distance to the Sun.

3. Optimal mission planning under nominal solar wind

The optimal orbit control problem is tackled in the current Section. Time-optimal orbits for rendezvous missions to Mars and Jupiter are obtained assuming nominal solar dynamic pressure. However, the solar wind uncertainty described in Section 2.3, is considered during mission planning by applying a control margin of 40%, equivalent to a saturation probability of 20%, to the nominal characteristic acceleration, $\overline{a}_c = 0.6\,\mathrm{m/s^2}$, used. This results in the characteristic acceleration $\tilde{a}_c = 0.36, \mathrm{m/s^2}$ used. The relation between saturation probability and control margin is shown in Figure 4. Since the time-dependency of the planets' position is not explicitly considered, this problem can be seen as an orbit-to-orbit transfer. However, due to the rotational symmetry of the problem (which comes from considering circular orbits), the orbit-to-orbit transfer becomes a planet-to-planet transfer simply by choosing the appropriate launch date.

First, the Optimal Control Problem (OCP) is formulated in Section 3.1. Then, it is solved by both an indirect (Section 3.2) and a direct (Section 3.3) approach. On the one hand, indirect methods apply optimality conditions first, which makes it possible to obtain local laws for the control variables converting the problem into a Two-Point Boundary Value Problem. On the other hand, direct transcription discretizes the problem in time, converting the set of optimization variables into a finite set of parameters, that is, a Non-Linear Programming (NLP) problem. Additionally, direct methods tend to be more stable and less dependent on initial conditions compared to indirect approaches. Therefore, the optimal orbits are first computed solving the NLP problem. Finally, the results obtained with both methodologies are compared in Section 3.4, in order to validate the solution and implementation of the direct method. This is particularly relevant as the same method is employed for the guidance phase described in Section 4.

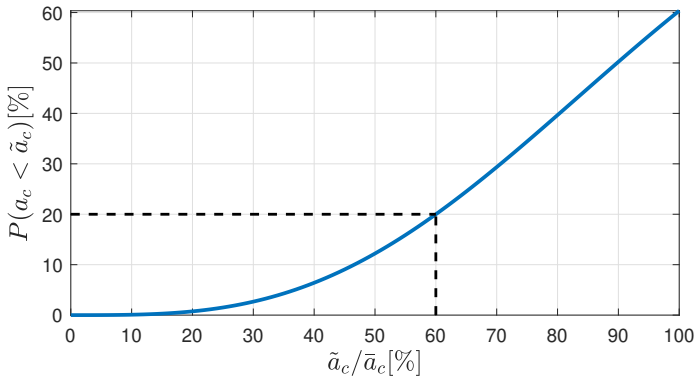

Figure 4: Saturation probability with respect to control margin

3.1. Optimal control problem formulation

The classical formulation for an OCP involves a cost function of the type

$$J\left[\boldsymbol{x}(\cdot),\boldsymbol{u}(\cdot),t_0,t_f\right]=\varphi\left[\boldsymbol{x}(t_0),t_0,\boldsymbol{x}(t_f),t_f\right]+\int_{t_0}^{t_f}\mathcal{L}\left[\boldsymbol{x}(t),\boldsymbol{u}(t),t\right]\mathrm{d}t \tag{6}$$

subject to the following state equations, path constraints and boundary conditions:

$$\boldsymbol{f}\left[\boldsymbol{x}(t),\boldsymbol{u}(t),t\right]=\dot{\boldsymbol{x}}, \tag{7}$$

$$\boldsymbol{h}\left[\boldsymbol{x}(t),\boldsymbol{u}(t),t\right]\leq 0, \tag{8}$$

$$\boldsymbol{g}\left[\boldsymbol{x}(t_0),t_0,\boldsymbol{x}(t_f),t_f\right]=0. \tag{9}$$

The bold notation is used to denote a vector. For this particular case, $\boldsymbol{x}=\{r,\theta,v_r,v_\theta\}$ and $\boldsymbol{u}=\{\tau,\alpha_n\}$. In this manner, the minimum time OCP can be expressed as

$$\begin{aligned}
&\min_{\tau,\alpha_n} \quad t_f\\
&\text{s.t.} \quad \underbrace{\begin{aligned}
\dot{r}&=v_r\\
\dot{\theta}&=\frac{v_\theta}{r}\\
\dot{v_r}&=\frac{v_\theta^2}{r}-\frac{\mu}{r^2}+\tau\frac{\tilde{a}_c}{2}\left(\frac{r_\oplus}{r}\right)\left(1+\cos^2\alpha_n\right)\\
\dot{v_\theta}&=-\frac{v_r v_\theta}{r}+\tau\frac{\tilde{a}_c}{2}\left(\frac{r_\oplus}{r}\right)\cos\alpha_n\sin\alpha_n
\end{aligned}}_{\text{state equations}}
\quad \underbrace{\begin{aligned}
0\leq\tau&\leq 1\\
-\alpha_n^{max}\leq\alpha_n&\leq\alpha_n^{max}
\end{aligned}}_{\text{path constraints}}
\quad \underbrace{\begin{aligned}
r(0)&=r_\oplus\\
\theta(0)&=0\\
v_r(0)&=0\\
v_\theta(0)&=v_\oplus\\
r(t_f)&=r_p\\
v_r(t_f)&=0\\
v_\theta(t_f)&=v_p,
\end{aligned}}_{\text{boundary conditions}}
\end{aligned} \tag{10}$$

where, without loss of generality, it has been imposed that $t_0=0$. The terms r_p and v_p, with $p=\mathrm{♂},\mathrm{♃}$, represent the distance from the Sun and the velocity of Mars and Jupiter respectively. Using astronomical units: $\mu=1$ AU UV^2, $r_\oplus=1$ AU, $r_{\mathrm{♂}}=1.5237$ AU, $r_{\mathrm{♃}}=5.2043$ AU, $v_{\mathrm{♂}}=0.8101$ UV, $v_{\mathrm{♃}}=0.4384$ UV. Lastly, the value of α_n is bounded by the previously introduced value $\alpha_n^{max}=70°$. The characteristic acceleration chosen for optimal planning is denoted as $\tilde{a}_c$. Note that the path constraints only affect the control variables. These constraints can be simply represented as $\boldsymbol{u}\in\mathcal{U}$, where $\mathcal{U}=\{\boldsymbol{u}\in\mathbb{R}^2:0\leq\tau\leq 1,-\alpha_n^{max}\leq\alpha_n\leq\alpha_n^{max}\}$ is the admissible control set.

Notice that in (10), no restriction is imposed on θ_f. That is because the launch date becomes "free to choose" under the assumed orbits of the planets (coplanar and circular) due to rotational symmetry. Once the problem is solved, the

launch date can be adjusted to effectively meet the corresponding planet when the spacecraft reaches its orbit. As a final remark, it should be acknowledged that due to the non-convexity of the problem constraints, the global nature of the optimal solutions found cannot be ensured, and the obtained solutions may be regarded as local optima.

3.2. Indirect approach

The difficulty of solving OCPs lies in the fact that input variables are functionals rather than discrete quantities, which makes it rather different compared to the standard parametric optimization problem. However, local laws that control parameters need to follow for the solution to be optimal can be found using indirect methods, and thus they transform the OCP into a Two Point Boundary Value Problem (TPBVP), which can then be solved numerically, although reaching convergence is not trivial. Indirect approaches have been previously used to characterize the performance of the E-sail [16, 19, 22, 23, 26].

To proceed, the state variables are expanded to the costate space, obtaining the set $\boldsymbol{\lambda} = \{\lambda_r, \lambda_\theta, \lambda_{v_r}, \lambda_{v_\theta}\}$, which satisfies the Euler-Lagrange equations $\dot{\lambda}_i = -\frac{\partial H}{\partial i}$, with $i = r, \theta, v_r, v_\theta$. The variable H is the Hamiltonian of the system, defined as $H = \mathcal{L} + \boldsymbol{\lambda}^\intercal \boldsymbol{f}$, where $\mathcal{L}$ is the integrand in (6).

The next step is to obtain the optimal control laws $\boldsymbol{u} = \boldsymbol{u}(\boldsymbol{x}, \lambda, t)$, which can be done by applying Pontryagin's Minimum Principle, that establishes a necessary condition (although not sufficient) for $\boldsymbol{u}$ to be optimal. Pontryagin's Minimum Principle states that for a cost function J to be minimized, the control parameters must minimize the Hamiltonian at every instant of time, i.e., $\boldsymbol{u}^\star = \underset{\boldsymbol{u}\in\mathcal{U}}{\operatorname{argmin}}\, H \quad \forall t \in [0, t_f]$, where * denotes optimality. For this particular system, the Hamiltonian is given by

$$\begin{aligned} H =& \lambda_r v_r + \lambda_\theta \frac{v_\theta}{r} + \lambda_{v_r}\left(\frac{v_\theta^2}{r} - \frac{\mu}{r^2}\right) - \lambda_{v_\theta}\frac{v_r v_\theta}{r} \\ &+ \tau\frac{\tilde{a}_c}{2}\left(\frac{r_\oplus}{r}\right)\left[\lambda_{v_r}\left(1+\cos^2\alpha_n\right) + \lambda_{v_\theta}\cos\alpha_n\sin\alpha_n\right]. \end{aligned} \tag{11}$$

If the optimal control is not located on the boundary of the admissible set, that is, $\boldsymbol{u}^\star \notin \partial\mathcal{U}$, the minimum value of a Hamiltonian must be a critical point. Therefore, $\frac{\partial H}{\partial \alpha_n}$ is computed, which yields

$$-\lambda_{v_r}\sin(2\alpha_n) + \lambda_{v_\theta}\cos(2\alpha_n) = 0, \tag{12}$$

obtaining two solutions, $\alpha_{n_1} = \frac{1}{2}\arctan 2\left(\lambda_{v_\theta}, \lambda_{v_r}\right)$ and $\alpha_{n_2} = \frac{1}{2}\arctan 2\left(-\lambda_{v_\theta}, -\lambda_{v_r}\right)$, where $\arctan 2$ is the two-argument inverse tangent function. Computing $\frac{\partial^2 H}{\partial \alpha_n^2}$ it is easy to see that the solution that corresponds to a minimum is α_{n_2}. However, that point could be outside of the admissible region, so the complete expression is

$$\alpha_n^\star = \begin{cases} \alpha_{n_2} & \text{if} \quad |\alpha_{n_2}| \le \alpha_n^{max}, \\ \alpha_n^{max}\cdot \operatorname{sgn}\left(\alpha_{n_2}\right) & \text{if} \quad |\alpha_{n_2}| > \alpha_n^{max}. \end{cases} \tag{13}$$

Regarding τ, a linear dependency is seen in H. Thus, to minimize the Hamiltonian, the best possible strategy for τ is to have minimum value when it is multiplied by a positive expression, and maximum in the opposite case.

$$\tau^\star = \begin{cases} 0 & \text{if} \quad \lambda_{v_r}\left(1+\cos^2\alpha_n^\star\right) + \lambda_{v_\theta}\cos\alpha_n^\star\sin\alpha_n^\star > 0, \\ 1 & \text{if} \quad \lambda_{v_r}\left(1+\cos^2\alpha_n^\star\right) + \lambda_{v_\theta}\cos\alpha_n^\star\sin\alpha_n^\star \le 0. \end{cases} \tag{14}$$

It can be computed that $\tau^\star$ switches to 0 whenever $\alpha_n^\star > \arccos\left(1/\sqrt{3}\right) \approx 54.7°$, effectively turning the E-sail off. This value coincides with the value of α_n that yields the maximum thrust cone angle $\alpha^{max} = \arctan\left(1/2\sqrt{2}\right)$ so, as conjectured in Section 2.1, there is no apparent reason for the sail pitch angle to go beyond 54.7°. Therefore, since $\alpha_n^{max} > \arccos\left(1/\sqrt{3}\right)$, saturation never takes place in the sail pitch angle and the optimal control law simply becomes

$$\alpha_n^\star = \frac{1}{2}\arctan2\left(-\lambda_{v_\theta}, -\lambda_{v_r}\right),$$
$$\tau^\star = \begin{cases} 0 & \text{if} \quad |\alpha_n| > \arccos\left(1/\sqrt{3}\right), \\ 1 & \text{if} \quad |\alpha_n| \leq \arccos\left(1/\sqrt{3}\right). \end{cases} \tag{15}$$

What is known as bang-bang control appears in τ due to its linear dependency with H, meaning that for a solution to be at least locally optimal, the throttle level must be at all times deactivated or at its maximum. Similar results are obtained in [16], although a slightly different thrust model is used. The full TPBVP is formulated below:

$$\begin{aligned}
\dot{r} =& v_r, \\
\dot{\theta} =& \frac{v_\theta}{r}, \\
\dot{v_r} =& \frac{v_\theta^2}{r} - \frac{\mu}{r^2} + \tau^\star \frac{\tilde{a}_c}{2}\left(\frac{r_\oplus}{r}\right)\left(1+\cos^2\alpha_n^\star\right), \\
\dot{v_\theta} =& -\frac{v_r\, v_\theta}{r} + \tau^\star \frac{\tilde{a}_c}{2}\left(\frac{r_\oplus}{r}\right)\cos\alpha_n^\star \sin\alpha_n^\star, \\
\dot{\lambda_r} =& \frac{\lambda_\theta\, v_\theta}{r^2} + \lambda_{v_r}\left(\frac{v_\theta^2}{r^2} - \frac{2\mu}{r^3}\right) - \lambda_{v_\theta}\frac{v_r\, v_\theta}{r^2} + \frac{\tau^\star\, \tilde{a}_c}{2\, r}\left(\frac{r_\oplus}{r}\right)\left[\lambda_{v_r}\left(1+\cos^2\alpha_n^\star\right) + \lambda_{v_\theta}\cos\alpha_n^\star \sin\alpha_n^\star\right], \\
\dot{\lambda_\theta} =& 0, \\
\dot{\lambda_{v_r}} =& -\lambda_r + \frac{\lambda_{v_\theta} v_\theta}{r}, \\
\dot{\lambda_{v_\theta}} =& -\frac{\lambda_\theta}{r} - \frac{2\,\lambda_{v_r} v_\theta}{r} + \frac{\lambda_{v_\theta} v_r}{r},
\end{aligned} \tag{16}$$

where $\alpha_n^\star$ and $\tau^\star$ are now optimal and given by (15). The system is subject to the following boundary conditions

$$\begin{aligned}
r(0) &= r_\oplus & r(t_f) &= r_p \\
\theta(0) &= 0 & \lambda_\theta(t_f) &= 0 \\
v_r(0) &= 0 & v_r(t_f) &= 0 \\
v_\theta(0) &= v_\oplus & v_\theta(t_f) &= v_p \\
& & H(t_f) &= -1.
\end{aligned} \tag{17}$$

This TPBVP is solved by implementing a shooting algorithm in the full state-costate system that also keeps track of the precise switching times of τ for numerical stability, similar to what is done in [56]. Several initial guesses are tried until a feasible solution is obtained.

3.3. Direct approach

The aim of this section is to convert this OCP into a Non-Linear Programming (NLP) problem, i.e. an optimization problem with a cost function subject to a set of algebraic equalities or inequalities. Thus, time is divided into N intervals $\boldsymbol{t} = \left[t_0, t_1, \ldots, t_N\right]^\intercal$. This solving method is known for being considerably more robust than indirect approaches, which highly depend on the initial guess. It has already been used for orbit optimization in low thrust spacecraft [57].

In this discretization, state variables are defined for each instant of time and control variables are assumed constant during each time interval, resulting in $4\,(N+1)$ state variables and $2N$ control variables. Taking into account that t_f is also a decision variable, and dividing the transfer in $N = 500$ intervals, the total number of NLP variables is 3005. Note that the value of N is relatively high because it considers not only the intervals for discretizing control but also

determines the number of intervals used for discretizing the dynamic equations, as the direct transcription approach is employed. Hence, a resolution higher than the one proposed in [58] is required.

Representing the values of the state variables at the instant t_k and of the control parameters in the interval $\left[t_k, t_{k+1}\right]$ as $\boldsymbol{x}_k$ and $\boldsymbol{u}_k$ respectively, dynamic constraints of the type $\boldsymbol{x}_{k+1} = \boldsymbol{f_d}\left(t_k, \boldsymbol{x}_k, \boldsymbol{u}_k\right)$ can be constructed by applying some integration scheme. A fourth-order Runge-Kutta is used in this work (details are skipped for simplicity). The boundary conditions can be added by setting $\boldsymbol{x}_0$ and $\boldsymbol{x}_N$ to the appropriate values. The path constraints $0 \leq \tau_k \leq 1$ and $-\alpha_n^{max} \leq \alpha_{n_k} \leq \alpha_n^{max}$ are set for each instant of time. With all these considerations, there are $4N + 7$ equality and $4N$ inequality constraints.

To solve the NLP problem, the algorithm Interior Point OPTimizer (IPOPT) [59] is used by means of the CasADi Toolbox for MATLAB [60]. As the problem constraints are not convex, one can not expect IPOPT to arrive to the global optimal solution, but rather a local one.

3.4. Optimal planning results

This section presents and compares the optimal trajectories obtained with both direct and indirect methods discussed in Sections 3.2 and 3.3. As already mentioned, a locally optimal solution is expected instead of a global, because of the non-convexity of the problem. However, indirect and direct methods can be compared to see if the solutions differ by much, giving insight into the quality of the solution, since both methods reach (local) optimality by means of different paths. It is useful to remember that, as demonstrated using Pontryagin's Minimum Principle, a bang-bang control in τ is expected.

The results obtained for missions to Mars and Jupiter are shown. A typical value of $\tilde{a}_c = 0.36$ mm/s^2 has been used for the characteristic acceleration. It should be noted that this value is lower than the maximum acceleration considered in other works [26, 61]. This discrepancy can be attributed to a combination of factors. On one hand, anticipating that a higher-than-usual payload fraction might be necessary for the interplanetary missions under consideration, a conservative value for the nominal characteristic acceleration is selected, being $\overline{a}_c = 0.6\,\mathrm{m/s^2}$. On the other hand, taking into account the PDF distribution presented in Section 2.3, a control margin of 40%, equivalent to a probability of saturation of 20%, has been applied to the nominal characteristic acceleration $\overline{a}_c$ selected. Consequently, the acceleration $\tilde{a}_c = 0.36\,\mathrm{m/s^2}$ considered for mission planning is obtained.

In Fig. 5, the resulting orbit to Jupiter using direct methods is shown, along with the evolution of state variables, control inputs, semi-major axis a and eccentricity e. Bang-bang structure in τ can be observed. The intervals in which thrust is off are called *coasting arcs*. Moreover, a tendency to return to distances of $\sim$ 1AU can also be seen, and this can be easily be explained by the fact that the closer the spacecraft is from the Sun, the higher the acceleration produced by the E-sail. The total duration of the mission is around 15 years.

A comparison between the direct and indirect approaches for the Mars transfer orbit is included in Fig. 6. As can be seen, the solutions obtained by both methods coincide, reaching Mars orbit in 1007 days. This does not guarantee that the solution is global, but helps validate both planning methods. More specifically, it helps justify the use of the direct method, since it can produce good results while being more reliable. Just for validation purposes, the transfer to Mars is also computed for $\tilde{a}_c = 1.00$ mm/s^2, resulting in 502 days, which is in line with typical transfer times reported in [26, 61].

Due to its higher stability, and given that the solutions obtained are similar between both methods, the direct approach is used for the guidance problem. Moreover, this direct transcription scheme makes the model predictive controller easier to implement. The values obtained for final time and polar angle are denoted as $t_{f,j}^{nom}$ and $\theta_{f,j}^{nom}$ (for $j = ♂, ♆$), and are used in Section 4.

4. Guidance strategies considering solar wind uncertainties

In this section the Sun variability is introduced along with its implications on saturation phenomena and control margins. Two approaches based on Model Predictive Control (MPC) are implemented, involving shrinking and receding time horizons. The selection of the propulsion strategy for control saturation periods and the impact of the cost function definition are studied. Based on the results obtained, the most promising strategy and options are identified.

4.1. The effect of solar wind perturbations

Hereinafter, the nominal characteristic acceleration $\overline{a}_c$ is defined as the acceleration of the spacecraft at 1 AU with nominal wind at maximum tether voltage, whereas the characteristic acceleration a_c considers a more realistic

dynamic pressure in which solar fluctuation is considered according to the model in Section 2.3. Similarly, $p_\oplus$ denotes the dynamic pressure and $\overline{p}_\oplus$ its mean.

Recalling (4), it is seen that force per unit length (and therefore the characteristic acceleration) is proportional to the tether grid voltage and to the square root of the dynamic pressure. Also, as seen in Section 2.3, the dynamic pressure randomly changes following a gamma distribution. Assuming that tethers can change their voltage instantaneously, and that the voltage change immediately translates into a change in the Coulomb's force generated by the E-sail (such a process' timescale is in the order of minutes, while the duration of interplanetary mission is in the order of years), one can compensate a change in $p_\oplus$ instantaneously with an appropriate modification of V_0 in order to maintain the needed spacecraft's acceleration. However, a problem arises when the dynamic pressure becomes so low that, not even with maximum voltage, the necessary acceleration can be obtained. Therefore, solar wind uncertainty may result in a saturation problem, preventing the optimal trajectory tracking and manifesting the necessity of a guidance strategy.

Since the characteristic acceleration of the spacecraft becomes variable, it is no longer useful to use the throttle level as a control input. Instead, an effective acceleration κ is defined, which can be expressed in terms of the throttle level, the nominal characteristic acceleration, and the dynamic pressure ratio as

$$\kappa = \tau a_c = \tau\, \overline{a}_c \sqrt{\frac{p_\oplus}{\overline{p}_\oplus}}. \tag{18}$$

If the same characteristic acceleration used in the optimal mission planning is utilized for guidance, saturation occurs each time $p_\oplus < \overline{p}_\oplus$. Therefore, it is convenient to define a *control margin* to reduce the probability of saturation. In fact, such a margin has already been considered considered in Section 3.4. Indeed, for the guidance strategy, a typical value of the characteristic acceleration of $\overline{a}_c = 0.6$ mm/s^2 is used [11], meaning that a control margin of 40% was left when computing the optimal planning, in which the characteristic acceleration was set to $\tilde{a}_c = 0.36$ mm/s^2. For reference, according to Fig. 4 which represents the saturation probability for a given control margin, it can be observed that not leaving control margin means that the probability of saturation is about 60%, while considering a 40% control margin (that is, $\tilde{a}_c = 0.6\,\overline{a}_c$) reduces the probability to around 20%. More control margin could be considered, but as a trade-off mission times get progressively larger.

4.2. Shrinking Horizon MPC Strategy

Since the dynamics of the system are known, one could predict the evolution of the spacecraft's orbit into the future given the values of the control variables, and assuming the dynamic pressure is known during that prediction horizon (it

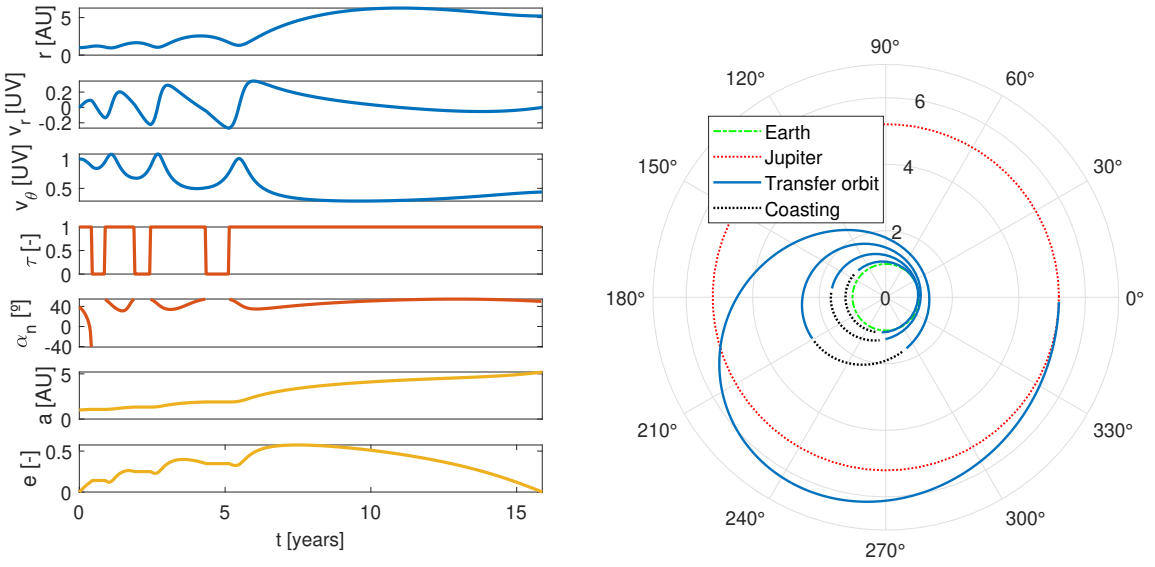

Figure 5: Evolution of variables (left) and trajectory (right) in a transfer orbit to Jupiter using a direct approach

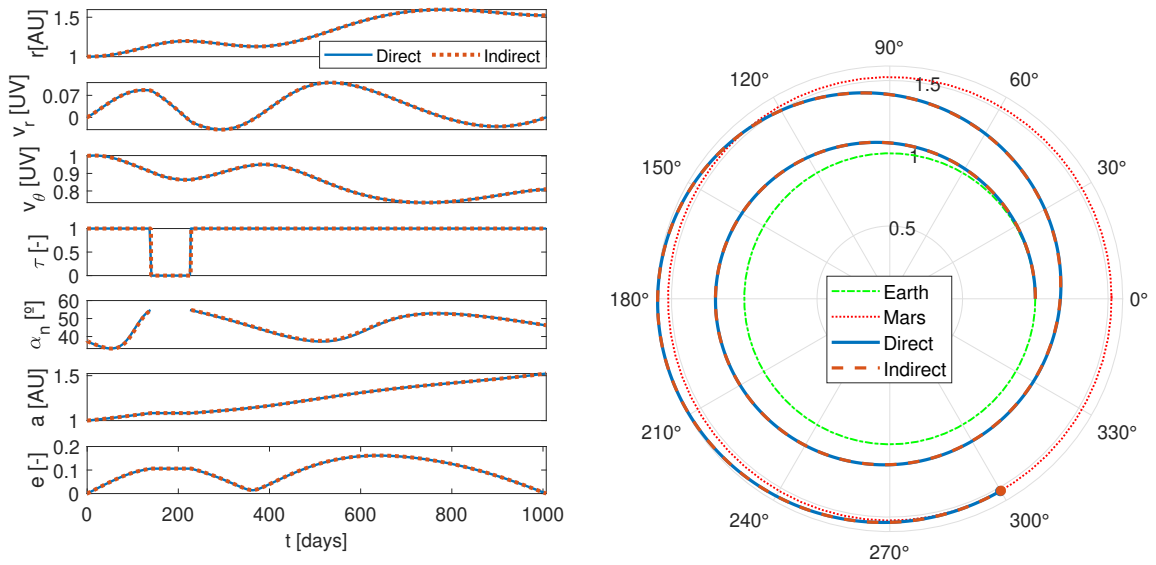

Figure 6: Evolution of variables (left) and trajectory (right) in a transfer orbit to Mars. Comparison between the direct and indirect solution

is indeed assumed constant). Then, some error measurement can be used to quantify how far the spacecraft has steered away from the reference trajectory. Of course, the dynamic pressure varies in the actual trajectory as opposed to the constant behaviour assumed when predicting into the future, but this method becomes more exact as the trajectory recalculation rate increases.

Using such orbit prediction, it is possible to formulate an OCP at a given mission time. The way in which the problem is posed here is by adding final constraints on the arrival time $t_{f,p}^{nom}$ and phase angle $\theta_{f,p}^{nom}$ obtained from the nominal planned orbit. Additionally, the modulus of the final velocity is fixed, while the cost function tries to minimize the square of final radial velocity. Even if such relaxation results in the velocity not exactly being that of the reached body, this small error can be handled by other specific propulsion systems to guarantee the rendez-vous.

The aim is to obtain the values for the control variables that minimizes such cost function, and the feedback loop is closed by recomputing the optimal controls with a certain frequency. The term "Shrinking Horizon" Model Predictive Control (SHMPC) comes from the fact that the arrival time is fixed, and the integration of the trajectory into the future is always performed up to that time instant, which implies that the remaining time keeps shrinking, as illustrated in Fig. 10(a).

Under the previous conditions and considering $N_{r,p}$ recalculations, the successive OCPs can be formulated as

$$
\begin{aligned}
\min_{\kappa,\alpha_n} \quad & v_r^2(t_f) \\
\text{s.t.} \quad & \underbrace{\begin{aligned} \dot{r} &= v_r \\ \dot{\theta} &= \frac{v_\theta}{r} \\ \dot{v}_r &= \frac{v_\theta^2}{r} - \frac{\mu}{r^2} + \frac{\kappa}{2}\left(\frac{r_\oplus}{r}\right)\left(1+\cos^2\alpha_n\right) \\ \dot{v}_\theta &= -\frac{v_r v_\theta}{r} + \frac{\kappa}{2}\left(\frac{r_\oplus}{r}\right)\cos\alpha_n \sin\alpha_n \end{aligned}}_{\text{state equations}} \quad \underbrace{\begin{aligned} 0 \le \kappa &\le \kappa^{max} \\ -\alpha_n^{max} \le \alpha_n &\le \alpha_n^{max} \end{aligned}}_{\text{path constraints}} \quad \underbrace{\begin{aligned} r(t_i) &= \hat{r}_i \\ \theta(t_i) &= \hat{\theta}_i \\ v_r(t_i) &= \hat{v}_{r_i} \\ v_\theta(t_i) &= \hat{v}_{\theta_i} \\ r(t_f) &= r_p \\ v^2(t_f) &= v_p^2 \\ t_f &= t_{f,p}^{nom} \\ \theta(t_f) &= \theta_{f,p}^{nom}, \end{aligned}}_{\text{boundary conditions}}
\end{aligned} \tag{19}
$$

where for $i = [1, ..., N_{r,p}]$, the solutions $r_i(t)$, $\theta_i(t)$, $v_{r_i}(t)$ and $v_{\theta_i}(t)$ define the time optimal partial trajectories for $t \in \left[t_i, t_f\right]$. Additionally, the final time t_f and the final polar angle $\theta(t_f)$ are now fixed and equal to $t_{f,p}^{nom}$ and $\theta_{f,p}^{nom}$ respectively, values obtained for the optimal planning presented in Section 3. Similarly, the final radius $r(t_f)$ is also fixed to r_p, thus ensuring the spacecraft reaches the planet. Finally, the value of t_i refers to the time at which the orbit is recalculated, an instant at which the state variables $\hat{r}_i$, $\hat{\theta}_i$, $\hat{v}_{r_i}$ and $\hat{v}_{\theta_i}$ are assumed to be known thanks to the navigation system. It is notable that they generally will differ from the optimal solution associated to the previous recalculation $r_{i-1}(t_i)$, $\theta_{i-1}(t_i)$, $v_{r_{i-1}}(t_i)$ and $v_{\theta_{i-1}}(t_i)$. In addition $p = ♂, ♆$ depends on whether the spacecraft aims to reach Mars or Jupiter, respectively.

The value of the maximum effective acceleration is $\kappa^{max} = a_c = \overline{a}_c \sqrt{p_\oplus / \overline{p}_\oplus}$, which changes over time. However, it must be known in order to solve the OCP. Thus, some assumption has to be made. In this work, where the trajectory is recomputed a total of $N_{r,♂} = 20$ times for Mars and $N_{r,♆} = 50$ times for Jupiter (so recalculation is performed every few months, hereinafter the instants at which recalculation is performed are noted t_i for $i = 1, ..., N_{r,♂}$ or $N_{r,♆}$) dynamic pressure is assumed constant and equal to the value measured at t_i for the next recalculation interval. Thus, $\kappa^{max,i}$ is indeed equal to a_c at the current time interval, but it may be convenient to limit it when predicting the trajectory in future intervals, to encourage the spacecraft to use as much acceleration as possible at the current time, since the problem becomes stiffer when approaching the target. Therefore, four distinct maximum values for effective acceleration in future time intervals (denoted as $\kappa^{max,+}$) are considered: (1) $\kappa^{max,+} = 0.6\,\overline{a}_c = 0.36$ mm/s^2 (that is, a 40% reduction from the real nominal characteristic acceleration, i.e., the value used in optimal planning), (2) $\kappa^{max,+} = 0.8\,\overline{a}_c = 0.48$ mm/s^2 (a 20% reduction, i.e., the mean between the real value and the used in orbit planning), (3) $\kappa^{max,+} = \overline{a}_c = 0.6$ mm/s^2 (no reduction), and (4) a linearly increasing value of $\kappa^{max,+}$ between 20% reduction and its full nominal value depending on the proximity to the end of the mission, that, is, $\kappa^{max,+} = [0.8 + 0.2\,(i-1)/(N_{r,p}-2)]\,\overline{a}_c$, where i is the current recalculation interval and $N_{r,p}$ the total number of recalculation intervals depending on whether the mission is to Mars or Jupiter. Note that i can be $N_{r,p} - 1$ at maximum, since at the last recalculation interval there are no future intervals.

Additionally, there is another issue that needs to be tackled. If the dynamic pressure at a given instant is low enough, or the spacecraft is sufficiently far from the reference trajectory, the solver may not find a solution. The impossibility of solving the OCP (even when relaxing the final conditions further) suggests the implementation of an alternative sub-optimal control law strategy during that interval. Such a strategy must minimize the deviation of the spacecraft trajectory with respect to the reference, to maximize the likelihood that the solver finds a solution in the next recalculation. It can be argued that setting the tethers voltage to its maximum (that is, applying full thrust) is convenient, since the infeasibility of the problem comes ultimately from a low value of $p_\oplus$. However, the angle in which the E-sail should position itself is not obvious. Therefore, three sub-optimal control laws are considered in this work: (1) full thrust (a^{max}) with $\alpha_n = \arccos(1/\sqrt{3})$, which provides maximum thrust cone angle, (2) full thrust with $\alpha_n = 0°$, maximizing radial acceleration (a_r^{max}), and (3) full thrust with $\alpha_n = 45°$, which maximizes tangential acceleration (a_θ^{max}). Because applying full thrust is convenient in these intervals, they are hereinafter denoted *full thrust arcs*.

4.2.1. Results for SHMPC

In order to compare the guidance strategies and quantify their performance given the solar wind perturbations, the following success and failure criteria are defined. A mission is considered successful (S) if the spacecraft is able to reach the planet's sphere of influence, while it is failed (F) depending on the miss distance, which is the distance at which the satellite remains from the planet, or $e = \|\boldsymbol{r}(t_f) - \boldsymbol{r}_p\|$. In the case of a Jupiter transfer, a fail is a miss of ten times (or more) the radius of Jupiter's sphere of influence. For a Mars transfer, since its sphere of influence is considerably smaller, failed missions are the ones with a miss distance of fifty times (or more) the radius of Mars' sphere of influence. These distances are considered high enough that no alternative propulsion system available can correct the error, hence the mission failure. A mission which ends with a miss distance in between the limits to be considered successful and failed is named partially successful, since it may be possible to reach the target, but employing considerable efforts from other propulsion systems.

Since acceleration saturation phenomena depends on $p_\oplus$ as shown in Section 4.1 and thus are stochastic, no deterministic metric of the performance of the strategies can be given. Instead, in order to statistically evaluate the different strategies presented in Section 4.2, a Monte Carlo analysis is conducted, simulating 100 missions for each of

Table 1
Monte Carlo results for SHMPC strategy for different $\kappa^{max,+}$ and α_n. The value $\bar{e}$ denotes the mean arrival error distance to the planet and σ_e its standard deviation in units of fail distance [UF]

		Mars				Jupiter			
$\kappa^{max,+}$	α_n such that	S [%]	F [%]	$\bar{e}$ [UF$_{\male}$]	σ_e [UF$_{\male}$]	S [%]	F [%]	$\bar{e}$ [UF$_{\female}$]	σ_e [UF$_{\female}$]
40% reduction	α^{max}	49	21	1.53	4.04	88	7	0.28	1.04
	a_r^{max}	22	55	3.21	4.18	57	19	0.57	1.32
	a_θ^{max}	43	33	2.04	3.97	76	14	0.39	1.13
20% reduction	α^{max}	52	9	0.31	0.66	90	8	0.28	0.92
	a_r^{max}	32	14	0.45	1.07	73	13	0.40	1.22
	a_θ^{max}	56	13	0.29	0.82	91	18	0.29	1.06
No reduction	α^{max}	18	27	0.86	1.36	68	28	1.09	1.92
	a_r^{max}	14	34	1.41	2.20	57	32	1.22	2.06
	a_θ^{max}	18	26	0.62	0.87	65	28	0.88	1.72
Linear increase	α^{max}	46	14	0.37	0.73	85	8	0.30	1.03
	a_r^{max}	28	14	1.00	2.79	65	10	0.83	1.35
	a_θ^{max}	41	13	0.48	1.02	80	11	0.55	0.98

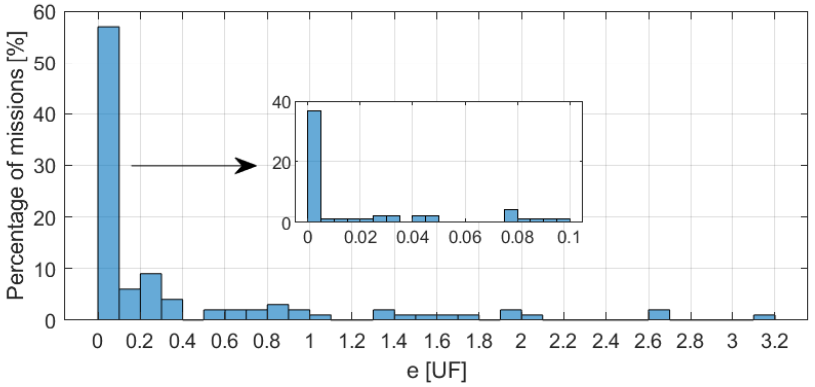

Figure 7: Histogram of the miss distance on missions to Mars with 20% $\kappa^{max,+}$ reduction and $\alpha_n\big|_{\alpha=\alpha^{max}}$

them, giving a total of $4 \cdot 3 \cdot 2 \cdot 100 = 2400$ simulations (four different $\kappa^{max,+}$ values and three full thrust arc strategies for missions to both Mars and Jupiter).

A summary of the results obtained is presented in Table 1, where the mean miss distance $\bar{e}$ (the average of the error distances e of each simulation) and its standard deviation σ_e are included to give an estimation on the precision and dispersion of the different strategies, and are expressed as multiples of the failing distance. Looking at the results, it becomes apparent that similar patterns emerge between missions to Mars and Jupiter regarding the most effective strategies. The key finding is that optimal results are achieved when a 20% reduction is considered for $\kappa^{max,+}$, and during full thrust arcs, thrust is applied in the direction that maximizes the sail cone angle ($\alpha_n = \arccos(1/\sqrt{3})$). The number of 100 simulations for each scenario was found to be a middle ground between computational effort and representativeness of the data. To check the representativeness, the outputs were recomputed for several random subsets of 50 of the 100 simulations, and the values obtained were sufficiently similar, justifying the chosen number of simulations.

As observed in Table 1, many missions to Mars fail. A histogram of the miss distance e of the simulations with the obtained optimal configuration is included in Fig. 7, while the spacecraft final position in each of the 100 missions is shown in Fig. 9, and an example of a successful mission using this guidance strategy can be seen in Fig. 8. For the obtained optimal configuration, the final radial velocity mean and standard deviation were found to be $\bar{v}_r(t_f) = 0.37$ km/s, $\sigma_{v_r(t_f)} = 1.05$ km/s. Although with a high variance, this mean value of the radial velocity is small enough for another more specific propulsion system to handle the rendez-vous.

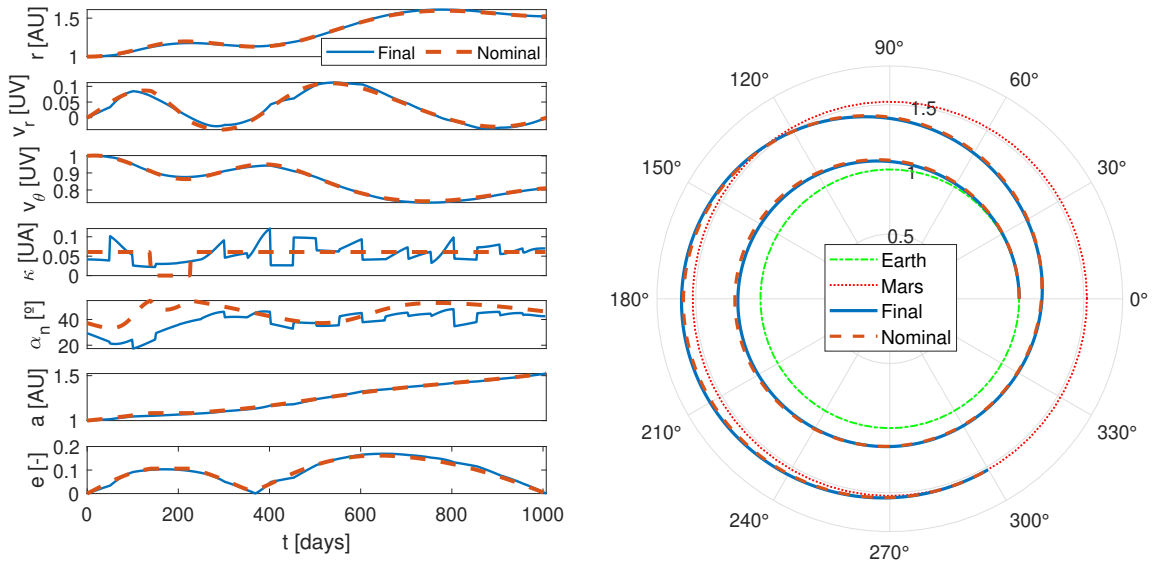

Figure 8: Evolution of variables (left) and trajectory (right) in a successful mission to Mars in the presence of uncertainty using SHMPC with 20% $\kappa^{max,+}$ reduction and $\alpha_n\big|_{\alpha=\alpha^{max}}$

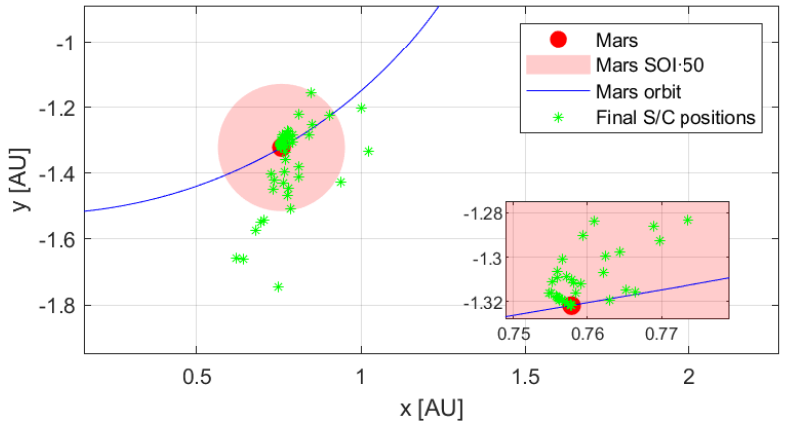

Figure 9: Final position error of the spacecraft in each of the Mars missions simulated for the 20% $\kappa^{max,+}$ reduction and $\alpha_n\big|_{\alpha=\alpha^{max}}$ SHMPC strategy

4.3. Receding Horizon MPC Strategy

In contrast to SHMPC approach presented in Section 4.2, in which arrival time is imposed, this section explores an alternative formulation that enables reaching the target planet in a greater time than initially planned, ($t_f > t_{f,p}^{nom}$) in exchange for robustness. To address this, a new optimization problem can be formulated with a cost function that includes not only the arrival position error, but also the position error at future points in time. Note that the reference orbit of the spacecraft is not only known for $t < t_f^{nom}$, but also for future values, because, given that a rendez-vous is desired, the spacecraft's reference orbit coincides with the planet's for $t > t_f^{nom}$. Therefore, these errors can be predicted by integrating the system into the future and comparing the obtained and the reference orbits. That means that now there are no arrival constraints, as they are incorporated in the cost function. The idea therefore is to check for the error at the nominal arrival time; if it is larger than an established value, the program continues and the spacecraft keeps

getting closer to the target, until a new check is made, then the process repeats. Once it gets sufficiently close (inside the sphere of influence), the mission ends.

This approach, called Receding Horizon Model Predictive Control (RHMPC), is schematically shown in Fig. 10(b) and allows for the predicting horizon to recede rather than shrink. When the trajectory is recomputed for the first time, the only instant at which the error is measured is the nominal arrival time t_f^{nom}. When recomputing at an arbitrary time $i = [1, ..., N_{r,p}]$, the current time is t_i, and the error is measured from t_f^{nom} until $t_f^{nom} + t_i$. That means that the controller is always computing the orbit up to a time of t_f^{nom} into the future, although the cost function accounts for position errors only for $t > t_f^{nom}$.

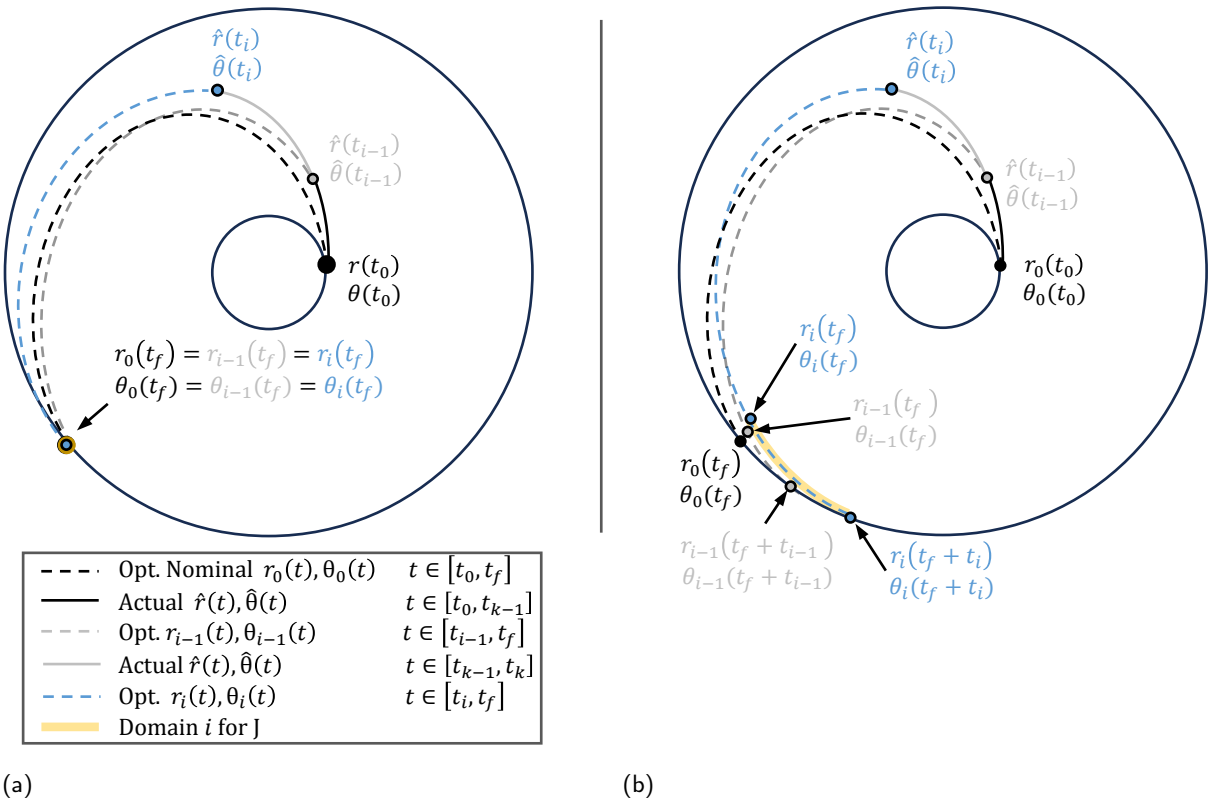

(a) (b)

Figure 10: Schematic view of (a) SHMPC strategy and (b) RHMPC strategy

The cost function formulated aims to minimize errors of the state variables. The following three position error functions are proposed:

$$\varepsilon_1(t) = r^2(t) + r_p^2 - 2\,r(t)\,r_p \cos\left(\theta(t) - \theta_p(t)\right), \tag{20}$$

$$\varepsilon_2(t) = \left(\frac{r(t) - r_p}{r_p}\right)^2 + (\theta(t) - \theta_p(t))^2, \tag{21}$$

$$\varepsilon_3(t) = \left(\frac{r(t) - r_p}{r_p}\right)^2 + c_1(\theta(t) - \theta_p(t))^2. \tag{22}$$

It can be observed that the first error function is the exact error distance, but it is more computationally expensive. The second is similar enough for small error values, and the third is a modification of the second in which radial and angular errors are differently weighted. For the third, a weight coefficient c_1 is fine-tuned following a brief study to assess its impact on the success rate. A value of $c_1 = 5$ is demonstrated to yield the optimal results.

Moreover, time-dependent weights are considered, to give priority to minimizing errors closer to the current time. The weight distribution $w_1(t)$ assumes a constant distribution, and $w_2(t)$ and $w_3(t)$ decreasing linear and quadratic distributions respectively. Therefore, given the definition of the cost function

$$J_{kl} = \int_{t_f^{nom}}^{t_f^{nom}+t_i} w_k(t)\epsilon_l(t)\mathrm{d}t, \tag{23}$$

a total of nine different cost functions are considered since $k = 1, 2, 3$ and $l = 1, 2, 3$.

With all these considerations the RHMPC strategy may be formulated for the successive $N_{r,p}$ OCPs as

$$\begin{aligned}
\min_{\kappa,\alpha_n} \quad & J_{kl} \qquad\qquad t \in \left[t_i, t_{f,p}^{nom} + t_i\right] \\
\text{s.t.} \quad & \underbrace{\begin{aligned} \dot{r} &= v_r \\ \dot{\theta} &= \frac{v_\theta}{r} \\ \dot{v}_r &= \frac{v_\theta^2}{r} - \frac{\mu}{r^2} + \frac{\kappa}{2}\left(\frac{r_\oplus}{r}\right)\left(1+\cos^2\alpha_n\right) \\ \dot{v}_\theta &= -\frac{v_r v_\theta}{r} + \frac{\kappa}{2}\left(\frac{r_\oplus}{r}\right)\cos\alpha_n \sin\alpha_n \end{aligned}}_{\text{state equations}} \quad \underbrace{\begin{aligned} 0 \le \kappa \le \kappa^{max} \\ -\alpha_n^{max} \le \alpha_n \le \alpha_n^{max} \end{aligned}}_{\text{path constraints}} \quad \underbrace{\begin{aligned} r(t_i) &= \hat{r}_i \\ \theta(t_i) &= \hat{\theta}_i \\ v_r(t_i) &= \hat{v}_{r_i} \\ v_\theta(t_i) &= \hat{v}_{\theta_i} \\ t_f - t_i &= t_{f,p}^{nom}, \end{aligned}}_{\text{boundary conditions}}
\end{aligned} \tag{24}$$

where the value of t_i refers to the time at which the orbit is recalculated, an instant at which the state variables $\hat{r}_i$, $\hat{\theta}_i$, $\hat{v}_{r_i}$ and $\hat{v}_{\theta_i}$ are assumed to be known thanks to the navigation system. Recalling the results from Section 4.2.1, a 20% reduction in κ^{max} is applied when recomputing the orbit to leave some control margin and minimize saturation-related problems.

4.3.1. Results for RHMPC

One hundred simulations are conducted for each of the nine cost functions, and for both Mars and Jupiter, resulting in a total of 1800 simulations. Examples of missions to Mars and Jupiter are shown in Fig. 12 and 13 respectively. The obtained results are included in Table 2, where $\Delta\bar{t}_f = (\bar{t}_f - t_f^{nom})/t_f^{nom}$ is the increment in percentage with respect to the nominal time, and $CV_{t_f} = \sigma_{t_f}/\bar{t}_f$ is the coefficient of variation of mission times, that is, the standard deviation divided by the mean.

Immediately, noticeable progress is seen with respect to results provided in Table 1. The spacecraft is able to reach the target every single time, and with the proper cost function tuning, the mean time increment of the mission are as low as 1.70% for Mars (for which a histogram is included in Fig. 11) and 0% for Jupiter, although these values can vary and more Monte Carlo simulations may be conducted to reduce the uncertainty of the results obtained. Nonetheless, a clear trend towards the use of ϵ_3 is seen, prioritizing angle error. In this case, according to Table 2, time-dependent weights $\omega_2(t)$ and $\omega_3(t)$ are not useful when ϵ_3 is used.

5. Missions to Mars using WSA-Enlil solar wind data

The goal of this section is to compute missions to Mars starting at different dates and using realistic solar wind data obtained from the WSA-Enlil model. The effectiveness of incorporating the RHMPC-based guidance approach, which has demonstrated superior performance, is substantiated by the mission success rate achieved under a solar wind uncertainty scenario.

5.1. Solar wind data extraction

For the solar wind data, the WSA-Enlil model is used [62]. The WSA-Enlil model uses a semi-empirical near-Sun module that approximates the solar wind in the vicinity of the Sun, and a three-dimensional magneto-hydrodynamic numerical model that propagates the resulting flow over greater distances. The data that emerge from this model are public and can be downloaded in *NetCDF* format. These data include proton density ρ_p and velocity v_p for a series of grid points in spherical coordinates, at various instants in time. The computation of the solar wind dynamic pressure is then immediate: $p_{dyn} = \rho_p v_p^2$.

Table 2
Monte Carlo results for RHMPC strategy for different cost functions. The value $\Delta\bar{t}_f$ denotes the mean mission time increment with respect to the nominal, and CV_{t_f} the coefficient of variation of the mission time. The value of $\#|_{\Delta t_f=0}$ indicates the percentage of missions in which time is not increased

		Mars			Jupiter		
Error	Weights	$\Delta\bar{t}_f$[%]	CV_{t_f}[%]	$\#\|_{\Delta t_f=0}$[%]	$\Delta\bar{t}_f$[%]	CV_{t_f}[%]	$\#\|_{\Delta t_f=0}$[%]
ε_1	w_1	6.20	11.20	70	0	0	100
	w_2	6.10	12.58	65	0.06	0.44	98
	w_3	7.80	15.44	69	0.26	1.31	96
ε_2	w_1	6.00	14.49	74	2.72	4.50	69
	w_2	3.50	6.98	73	4.54	8.95	73
	w_3	4.30	9.39	74	0	0	100
ε_3	w_1	1.70	6.42	90	0	0	100
	w_2	4.90	12.52	77	0	0	100
	w_3	12.90	22.57	71	0	0	100

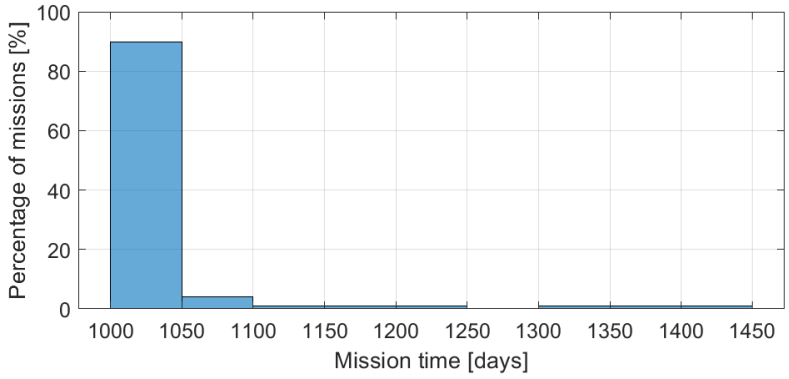

Figure 11: Histogram of Mars missions duration using RHMPC and considering the cost function J_{13}

There are a couple of reasons of why missions to Jupiter are not conducted in this section. As seen in Section 3.4, a mission to Jupiter with a characteristic acceleration of $\tilde{a}_c = 0.36$ mm/s^2 takes approximately 15 years to complete. However, WSA-Enlil cannot provide data prior to 2013, so the necessary data is simply unavailable. The other reason is that WSA-Enlil can provide measures for distances to the Sun between 0.1 and 1.7AU. Therefore, there is no data for the region in which Jupiter lies, at 5.2AU from the Sun.

Solar wind data is downloaded from July 2019 onwards until June 2023, that is, four years of data. Taking into account that the nominal mission time to Mars is of around 3 years, the collected data is enough. Then, 12 different missions are conducted, each starting on the first day of every month from July 2019 to June 2020.

5.2. Implementation and results

The way in which the realistic solar wind data is implemented into the simulation is straight-forward. As explained in Section 4.3, at a given instant t_i, the controller recomputes the orbit that minimizes the cost function, from which the control actions are obtained. For such computation, the mean value of the solar wind dynamic pressure is considered, plus a 20% reduction for control margin purposes. Then, the system is integrated into the future using the control actions previously obtained, and now applying the actual WSA-Enlil data for the solar wind dynamic pressure. This integration is carried out until instant t_{i+1}, in which the process is repeated.

In Fig. 14, all the twelve missions are shown overlapped in the same picture. On the left, the evolution of the state and control variables is shown, while on the right the evolution of the dynamic pressure is presented. There are several things to notice in this figure. Trajectories start being very close to each other, since not sufficient time has passed for the dynamic pressure uncertainty to propagate and produce noticeable deviations. Towards the end, and specially

each time the on-line orbit recalculation is performed, trajectories start to deviate since the spacecraft are located in slightly different places, difference that can make a noticeable change in terms of the optimal control computation. Nevertheless, all twelve missions are capable of reaching Mars within the planned time, which evidences the suitability of this guidance algorithm.

Regarding the dynamic pressure, one can compare its evolution with respect to what is expected, that is, the mean value. From (1) it follows that the E-sail acceleration is inversely proportional to the Sun distance, while from (4) the acceleration is proportional to the square root of the dynamic pressure. Combining both relations, it is derived that the

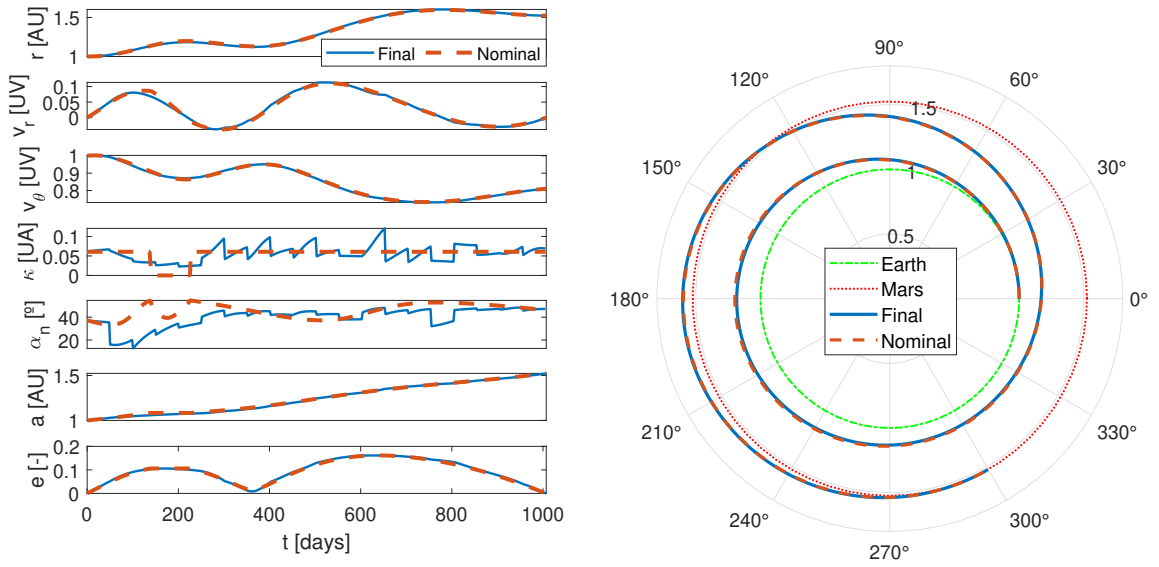

Figure 12: Evolution of variables (left) and trajectory (right) in a mission to Mars in the presence of uncertainty using RHMPC and considering the cost function J_{13}.

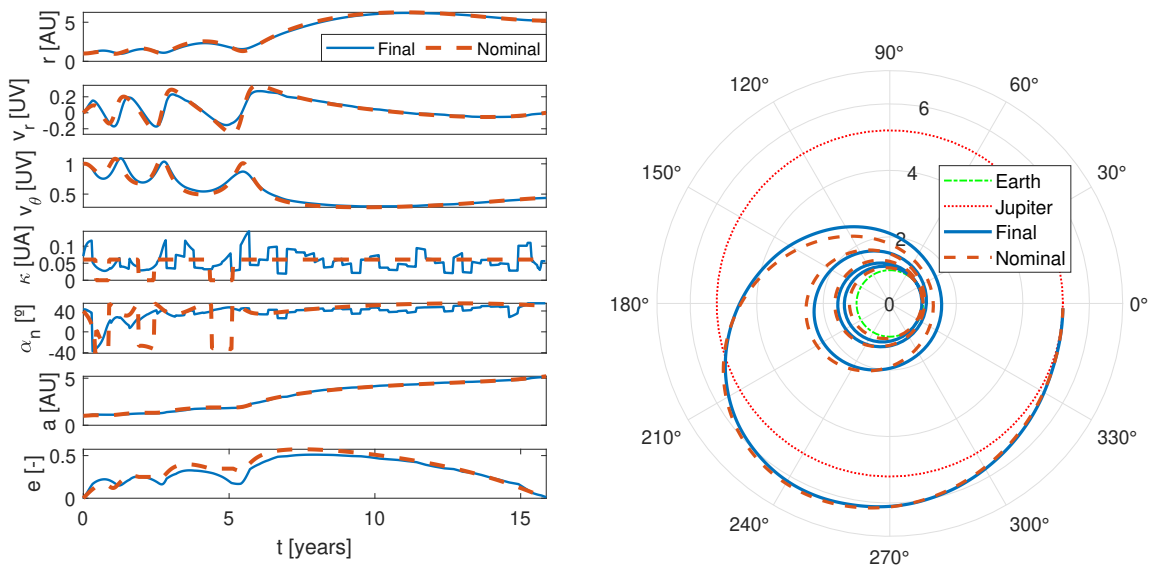

Figure 13: Evolution of variables (left) and trajectory (right) in a mission to Jupiter in the presence of uncertainty using RHMPC and considering the cost function J_{33}

dynamic pressure is inversely proportional to the Sun distance squared, so its mean value $\overline{p}_{dyn}$ can be obtained for any r knowing the mean value at 1AU, that is,

$$\overline{p}_{dyn} = \left(\frac{r_{\oplus}}{r}\right)^2 \overline{p}_{\oplus}. \tag{25}$$

The mean value, $\overline{p}_{dyn}$ is shown with the dashed black line on the dynamic pressure evolution on Fig. 14, and it is clearly concluded that the dynamic pressures obtained from WSA-Enlil throughout the missions follow the expected mean.

6. Conclusions

E-Sails, a novel spacecraft propulsion system harnessing energy from solar wind protons that have been considered straightforward for interplanetary missions, necessitate further exploration into active guidance strategies due to the significant variability of the solar wind, a topic previously under-studied. This work presents two main approaches based on Model Predictive Control are developed and compared: Shrinking Horizon and Receding Horizon. The consideration of variations on the cost functions and the guiding strategies are proposed and evaluated.

Analyzing the results for missions to Mars and Jupiter, it is demonstrated that the Receding Horizon Model Predictive Control approach is superior to the Shrinking Horizon Model Predictive Control strategy. However, the results obtained for Shrinking Horizon Model Predictive Control, allow to draw two main conclusions. On one hand, the selection of the margin applied to the effective acceleration for the successive trajectory recalculation notably affect the rate of success of the mission. On the other hand, the impact of the sub-optimal control law considered for the intervals where the control is under saturation due to the severe decay of solar pressure, is recognized. In regards to the results obtained for Receding Horizon Model Predictive Control strategy, the spacecraft is able to reach the target every time. For Jupiter transfer missions, a 100% success rate is achieved and the nominal planning arrival time satisfied. In the case of mission with destination to Mars, the best results are obtained by considering the J_{13} cost function. In 90% of the cases, the planet is reached at the nominal planning arrival time, whereas for the remaining 10%, the mission arrival times is slightly increased, on average by 1.70%, compared to the nominal planning. In addition, the effectiveness of considering the cost function ϵ_3, giving extra weight to the error on the tangential velocity, can be outlined. To further validate the utility of the Receding Horizon Model Predictive Control guidance strategy, twelve different Mars missions are computed using solar wind historical data obtained from the WSA-Enlil model. In all of the missions, the spacecraft successfully reached the target, confirming the robustness of Receding Horizon Model Predictive Control

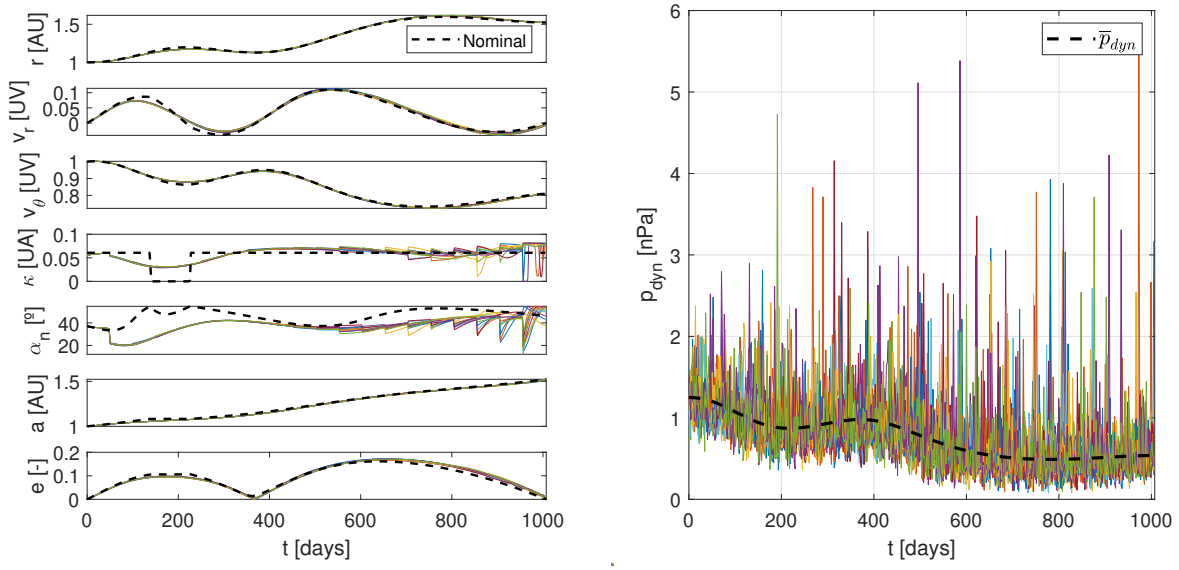

Figure 14: Evolution of variables (left) and solar dynamic pressure (right) in a mission to Mars using WSA-Enlil solar wind data and RHMPC considering the cost function J_{13}

under accurate sun wind fluctuations. Therefore, the previous considerations allows to identify E-sails as a feasible propellantless alternative for interplanetary missions, provided that the programmed guidance strategy is appropriate.

Nevertheless, more in-depth analyses of the problem need to be addressed, for instance by considering the real orbits of the planets, opting for a more complex propulsive model, or addressing some other interplanetary missions (for example, missions to inner planets or asteroids), among other possibilities. It is also left as future work the parameterization of the trajectories, the study of a robust formulation of the MPC (an example on the rendezvous domain is [40]), asymptotic stability guarantees, and characteristics of the terminal region and terminal cost of the controller. Stochastic formulations may also be of interest.

Acknowledgement

The authors gratefully acknowledge support by grant TED2021-132099B-C33 funded by MCIN/AEI/10.13039/501100011033 and by "European Union NextGenerationEU/PRTR."

CRediT authorship contribution statement

Javier Urrios: Conceptualization of this study, Methodology, Software. **Guillermo Pacheco-Ramos:** Conceptualization of this study, Methodology, Software. **Rafael Vazquez:** Conceptualization of this study, Methodology, Software.

References

[1] M. Urbanczyk, Solar Sails - A realistic propulsion for spacecraft, Tech. rep. (1967).
[2] F. Tsander, Problems of flight by jet propulsion: interplanetary flights, NASA technical translation, Tech. Rep, 1964.
[3] D. A. Spencer, B. Betts, J. M. Bellardo, A. Diaz, B. Plante, J. R. Mansell, The Lightsail 2 solar sailing technology demonstration, Advances in Space Research 67 (9) (2021) 2878–2889. doi:10.1016/j.asr.2020.06.029.
[4] O. Mori, H. Sawada, R. Funase, et al., First solar power sail demonstration by IKAROS, Transactions of the Japan Society for Aeronautical and Space Sciences, Aerospace Technology Japan 8 (ists27) (2010) To_4_25–To_4_31. doi:10.2322/tastj.8.To_4_25.
[5] W. K. Wilkie, Overview of the NASA Advanced Composite Solar Sail System (ACS3) Technology Demonstration Project, AIAA Scitech Forum (2021). doi:10.2514/6.2021-1260.
[6] J. B. Pezent, R. Sood, A. Heaton, K. Miller, L. Johnson, Preliminary trajectory design for NASA's Solar Cruiser: A technology demonstration mission, Acta Astronautica 183 (2021) 134–140. doi:10.1016/j.actaastro.2021.03.006.
[7] R. M. Zubrin, D. G. Andrews, Magnetic sails and interplanetary travel, Journal of Spacecraft and Rockets 28 (2) (1991) 197–203. doi:10.2514/3.26230.
[8] P. Janhunen, Electric sail for spacecraft propulsion, Journal of Propulsion and Power 20 (4) (2004) 763–764. doi:10.2514/1.8580.
[9] P. Janhunen, A. Sandroos, Simulation study of solar wind push on a charged wire: basis of solar wind electric sail propulsion, in: Annales Geophysicae, Vol. 25, Copernicus GmbH, 2007, pp. 755–767. doi:10.5194/angeo-25-755-2007.
[10] P. Janhunen, Photonic spin control for solar wind electric sail, Acta Astronautica 83 (2013) 85–90. doi:10.1016/j.actaastro.2012.10.017.
[11] M. Bassetto, L. Niccolai, A. A. Quarta, G. Mengali, A comprehensive review of Electric Solar Wind Sail concept and its applications, Progress in Aerospace Sciences 128 (2022) 100768. doi:10.1016/j.paerosci.2021.100768.
[12] G. Li, Z. H. Zhu, C. Du, Stability and control of radial deployment of electric solar wind sail, Nonlinear Dynamics 103 (1) (2021) 481–501. doi:10.1007/s11071-020-06067-7.
[13] P. Janhunen, P. Toivanen, J. Envall, et al., Overview of electric solar wind sail applications, Proceedings of the Estonian Academy of Sciences 63 (2) (2014) 267. doi:10.3176/proc.2014.2S.08.
[14] M. Huo, G. Mengali, A. A. Quarta, Electric sail thrust model from a geometrical perspective, Journal of Guidance, Control, and Dynamics 41 (3) (2018) 735–741. doi:10.2514/1.G003169.
[15] K. Yamaguchi, K. Miyata, Orbital maneuvering of electric solar wind sail based on an advanced solar wind force model, Acta Astronautica 166 (2020) 417–430. doi:10.1016/j.actaastro.2019.10.001.
[16] G. Mengali, A. A. Quarta, P. Janhunen, Electric sail performance analysis, Journal of Spacecraft and Rockets 45 (1) (2008) 122–129. doi:10.2514/1.31769.
[17] L. Niccolai, A. A. Quarta, G. Mengali, M. Bassetto, Trajectory Analysis of a Zero-Pitch-Angle E-Sail with Homotopy Perturbation Technique, Journal of Guidance, Control, and Dynamics 46 (4) (2023) 734–741. doi:10.2514/1.G007219.
[18] M. Bassetto, A. A. Quarta, G. Mengali, Locally-optimal electric sail transfer, Proceedings of the Institution of Mechanical Engineers, Part G: Journal of Aerospace Engineering 233 (1) (2019) 166–179. doi:10.1177/0954410017728975.
[19] A. A. Quarta, G. Mengali, P. Janhunen, Electric sail option for cometary rendezvous, Acta Astronautica 127 (2016) 684–692. doi:10.1016/j.actaastro.2016.06.020.
[20] L. Niccolai, Optimal deep-space heliocentric transfers with an electric sail and an electric thruster, Advances in Space Research (2023). doi:10.1016/j.asr.2023.08.047.

[21] M. Huo, R. Jin, L. Yang, N. Qi, Indirect Optimization of Optimal Continuous Trajectory for Electric Sails With Refined Thrust Model in the Multi-Target Exploration Scenario, IEEE Transactions on Aerospace and Electronic Systems 59 (4) (2023) 4274–4288. doi:10.1109/TAES.2023.3242639.

[22] A. A. Quarta, G. Mengali, P. Janhunen, Electric sail for a near-Earth asteroid sample return mission: case 1998 KY26, Journal of Aerospace Engineering 27 (6) (2014) 04014031. doi:10.1061/(ASCE)AS.1943-5525.0000285.

[23] A. A. Quarta, G. Mengali, Electric sail mission analysis for outer solar system exploration, Journal of Guidance, Control, and Dynamics 33 (3) (2010) 740–755. doi:10.2514/1.47006.

[24] M. Huo, Z. Fan, J. Qi, N. Qi, D. Zhu, Fast Analysis of Multi-Asteroid Exploration Mission Using Multiple Electric Sails, Journal of Guidance, Control, and Dynamics 46 (5) (2023) 1015–1022. doi:10.2514/1.G006972.

[25] M. Bassetto, L. Boni, G. Mengali, A. A. Quarta, Electric sail phasing maneuvers with radial thrust, Acta Astronautica 179 (2021) 99–104. doi:10.1016/j.actaastro.2020.10.025.

[26] A. Caruso, L. Niccolai, G. Mengali, A. A. Quarta, Electric sail trajectory correction in presence of environmental uncertainties, Aerospace Science and Technology 94 (2019) 105395. doi:10.1016/j.ast.2019.105395.

[27] M. Bassetto, A. A. Quarta, G. Mengali, Thrust model and guidance scheme for single-tether E-sail with constant attitude, Aerospace Science and Technology 142 (2023) 108618. doi:10.1016/j.ast.2023.108618.

[28] G. Li, Z. H. Zhu, C. Du, S. Meguid, Characteristics of coupled orbital-attitude dynamics of flexible electric solar wind sail, Acta Astronautica 159 (2019) 593–608. doi:10.1016/j.actaastro.2019.02.009.

[29] T. D. Lillian, Modal Analysis of Electric sail, Acta Astronautica 185 (2021) 140–147. doi:10.1016/j.actaastro.2021.05.003.

[30] M. Bassetto, G. Mengali, A. A. Quarta, Attitude dynamics of an electric sail model with a realistic shape, Acta Astronautica 159 (2019) 250–257. doi:10.1016/j.actaastro.2019.03.064.

[31] S. Zeng, W. Fan, H. Ren, Attitude control for a full-scale flexible electric solar wind sail spacecraft on heliocentric and displaced non-Keplerian orbits, Acta Astronautica 211 (2023) 734–749. doi:10.1016/j.actaastro.2023.07.005.

[32] L. Huang, H. Wen, L. Cheng, S. Xu, Nonlinear model predictive control for attitude maneuver of a barbell electric sail through voltage regulation, Acta Astronautica 179 (2021) 146–152. doi:10.1016/j.actaastro.2020.10.028.

[33] X. Ma, L. Huang, H. Wen, S. Xu, Deep learning-based nonlinear model predictive control of the attitude manoeuvre of a barbell electric sail through voltage regulation, Acta Astronautica 195 (2022) 118–128. doi:10.1016/j.actaastro.2022.02.018.

[34] G. Li, Z. H. Zhu, C. Du, Flight dynamics and control strategy of electric solar wind sails, Journal of Guidance, Control, and Dynamics 43 (3) (2020) 462–474. doi:10.2514/1.G004608.

[35] J. Sun, E. Chen, T. Chen, D. Jin, Spin dynamics of a long tethered sub-satellite system in geostationary orbit, Acta Astronautica 195 (2022) 12–26. doi:10.1016/j.actaastro.2022.02.026.

[36] C. Du, Z. H. Zhu, G. Li, Analysis of thrust-induced sail plane coning and attitude motion of electric sail, Acta Astronautica 178 (2021) 129–142. doi:10.1016/j.actaastro.2020.09.001.

[37] G. Pacheco-Ramos, D. Garcia-Vallejo, R. Vazquez, Formulation of a high-fidelity multibody dynamical model for an electric solar wind sail, International Journal of Mechanical Sciences 256 (2023) 108466. doi:10.1016/j.ijmecsci.2023.108466.

[38] L. Niccolai, A. Anderlini, G. Mengali, A. A. Quarta, Impact of solar wind fluctuations on electric sail mission design, Aerospace Science and Technology 82-83 (2018) 38–45. doi:10.1016/j.ast.2018.08.032.

[39] P. K. Toivanen, P. Janhunen, Electric sailing under observed solar wind conditions, Astrophysics and Space Sciences Transactions 5 (1) (2009) 61–69. doi:10.5194/astra-5-61-2009.

[40] F. Gavilan, R. Vazquez, E. F. Camacho, Chance-constrained model predictive control for spacecraft rendezvous with disturbance estimation, Control Engineering Practice 20 (2) (2012) 111–122. doi:10.1016/j.conengprac.2011.09.006.

[41] J. C. Sanchez, F. Gavilan, R. Vazquez, C. Louembet, A flatness-based predictive controller for six-degrees of freedom spacecraft rendezvous, Acta Astronautica 167 (2020) 391–403. doi:10.1016/j.actaastro.2019.11.026.

[42] F. Gavilan, R. Vazquez, E. F. Camacho, Robust Model Predictive Control for Spacecraft Rendezvous with Online Prediction of Disturbance Bound, in: Proceedings of AGNFCS'09, Samara, Russia, 2009.

[43] J. C. Sanchez, F. Gavilan, R. Vazquez, Chance-constrained model predictive control for near rectilinear halo orbit spacecraft rendezvous, Aerospace Science and Technology 100 (2020) 105827. doi:10.1016/j.ast.2020.105827.

[44] Y. Zhang, M. Cheng, B. Nan, S. Li, Stochastic trajectory optimization for 6-DOF spacecraft autonomous rendezvous and docking with nonlinear chance constraints, Acta Astronautica 208 (2023) 62–73. doi:10.1016/j.actaastro.2023.04.004.

[45] C. E. Oestreich, R. Linares, R. Gondhalekar, Tube-Based Model Predictive Control with Uncertainty Identification for Autonomous Spacecraft Maneuvers, Journal of Guidance, Control, and Dynamics 46 (1) (2023) 6–20. doi:10.2514/1.G006438.

[46] M. Tiwari, R. Prazenica, T. Henderson, Direct adaptive control of spacecraft near asteroids, Acta Astronautica 202 (2023) 197–213. doi:10.1016/j.actaastro.2022.10.014.

[47] D. Ge, X. Chu, Robust learning for collision-free trajectory in space environment with limited a priori information, Acta Astronautica 187 (2021) 281–294. doi:10.1016/j.actaastro.2021.06.038.

[48] A. Zavoli, L. Federici, Reinforcement learning for robust trajectory design of interplanetary missions, Journal of Guidance, Control, and Dynamics 44 (8) (2021) 1440–1453. doi:10.2514/1.G005794.

[49] K. Oguri, J. W. McMahon, Robust spacecraft guidance around small bodies under uncertainty: Stochastic optimal control approach, Journal of Guidance, Control, and Dynamics 44 (7) (2021) 1295–1313. doi:10.2514/1.G005426.

[50] C. Greco, S. Campagnola, M. Vasile, Robust space trajectory design using belief optimal control, Journal of Guidance, Control, and Dynamics 45 (6) (2022) 1060–1077. doi:10.2514/1.G005704.

[51] X. Jiang, S. Li, Mars entry trajectory planning using robust optimization and uncertainty quantification, Acta Astronautica 161 (2019) 249–261. doi:10.1016/j.actaastro.2019.05.033.

[52] M. Huo, G. Mengali, A. A. Quarta, Optimal planetary rendezvous with an electric sail, Aircraft Engineering and Aerospace Technology: An International Journal 88 (4) (2016) 515–522. doi:10.1108/AEAT-01-2015-0012.

[53] P. Janhunen, P. K. Toivanen, Polkko, et al., Invited article: Electric solar wind sail: Toward test missions, Review Of Scientific Instruments 81 (11) (2010). doi:10.1063/1.3514548.

[54] D. Colburn, C. Sonett, Discontinuities in the solar wind, Space Science Reviews 5 (4) (1966) 439–506. doi:10.1007/BF00240575.

[55] L. Niccolai, A. Anderlini, G. Mengali, A. A. Quarta, Electric sail displaced orbit control with solar wind uncertainties, Acta Astronautica 162 (2019) 563–573. doi:10.1016/j.actaastro.2019.06.037.

[56] C. Zhang, F. Topputo, F. Bernelli-Zazzera, Y.-S. Zhao, Low-thrust minimum-fuel optimization in the circular restricted three-body problem, Journal of Guidance, Control, and Dynamics 38 (8) (2015) 1501–1510. doi:10.2514/1.G001080.

[57] F. Topputo, C. Zhang, Survey of direct transcription for low-thrust space trajectory optimization with applications, Abstract and Applied Analysis 2014 (2014) 1–15. doi:10.1155/2014/851720.

[58] M. Otten, C. McInnes, Near minimum-time trajectories for solar sails, Journal of Guidance Control and Dynamics 24 (05 2001). doi:10.2514/2.4758.

[59] A. Wächter, L. T. Biegler, On the implementation of an interior-point filter line-search algorithm for large-scale nonlinear programming, Mathematical programming 106 (2006) 25–57. doi:10.1007/s10107-004-0559-y.

[60] J. A. E. Andersson, J. Gillis, G. Horn, J. B. Rawlings, M. Diehl, CasADi – A software framework for nonlinear optimization and optimal control, Mathematical Programming Computation 11 (1) (2019) 1–36. doi:10.1007/s12532-018-0139-4.

[61] A. A. Quarta, G. Mengali, Minimum-time trajectories of electric sail with advanced thrust model, Aerospace Science and Technology 55 (2016) 419–430. doi:10.1016/j.ast.2016.06.020.

[62] V. Pizzo, G. Millward, A. Parsons, D. Biesecker, S. Hill, D. Odstrcil, Wang-Sheeley-Arge-Enlil cone model transitions to operations, Space Weather 9 (3) (2011) 03004. doi:10.1029/2011SW000663.